Analysis of Inviscid Simulations for the Study of Supersonic Retropropulsion

Noël M. Bakhtian[*]

Stanford University, Stanford, CA, 94305

Michael J. Aftosmis[†]

NASA Ames Research Center, Moffett Field, CA, 94035

Supersonic retropropulsion (SRP) has been proposed as a candidate enabling technology for future high-mass Mars missions. Fast, automated, and robust computations are useful for investigating the preliminary design space and are necessary for eventual optimization of such a system. This paper examines the prediction capability of a steady Cartesian Euler solver with adjoint-based adaptive mesh refinement when applied to SRP flows. Comparisons to several wind tunnel data sets and related Navier-Stokes simulations are made, concentrating on central (1-nozzle) and peripheral (3- and 4-nozzle) configurations at Mach numbers from 3.48 to 4.60, angles of attack ranging from $0°$ to $20°$, and thrust coefficients from 0.4 to 3. The adjoint-adapted, steady, inviscid simulations show good agreement of both detailed surface pressures and complex off-body flow features, demonstrating the ability to capture relevant SRP flow physics and predict loads.

I.   Introduction

WITH sample-return and manned missions on the horizon for Mars exploration, the ability to decelerate high-mass systems upon arrival at a planet's surface has become a research priority. Mars' thin atmosphere necessitates the use of entry, descent, and landing (EDL) systems to aid in deceleration to sufficiently low terminal descent velocities.[1,2] Supersonic retropropulsion (SRP), the use of propulsive deceleration during the supersonic portion of entry (Fig. 1), is currently being developed to address the challenge of an orders-of-magnitude increase in landed mass capability required for future Mars exploration.[3]

1.   Supersonic Retropropulsion (SRP) Development

The use of retropropulsive jets in a supersonic freestream as a means of atmospheric deceleration is a relatively new field. Several historic works from the Viking mission era proposed the concept and completed experimental work leading to a preliminary understanding of SRP flow physics.[4–11] More recently, studies on aerospike-like[12] single, opposing jets for the purpose of drag reduction and amelioration of surface heating have contributed SRP data in the form of CFD results[13–17] based on historic experimental work.[18–20] A survey of these early efforts is given in Ref. 21. Recently resurfacing as an atmospheric deceleration technique,[1,2,22–25] supersonic retropropulsion is featured in four of eight potential high-mass NASA EDL architectures,[26] establishing the need for SRP technology advancement.

SRP development will rely heavily on CFD capabilities for initial exploratory studies of the design space, database completion based on Mars conditions, and performing specific aerodynamic and aerothermal calculations.[3] CFD capabilities are currently being matured through a series of validation studies, establishing best practices for SRP flow field prediction.[27–40] These preliminary CFD solutions are anchored to both wind tunnel testing completely specifically
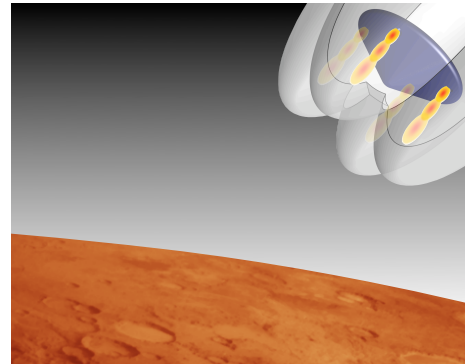

Figure 1.   Illustration of SRP for atmospheric deceleration.

for this CFD simulation development[30, 33, 34, 41, 42] and early experimental data.[8, 9, 16, 43] With the exception of brief studies in Refs. 27, 29, and 32, recent CFD development has focused on viscous numerical methods. Inviscid, steady modeling techniques, in contrast, require less computational effort by orders of magnitude, enabling rapid analysis of the myriad simulations required for design and optimization. This work represents the first study devoted to inviscid numerical validation for SRP flows.

This paper examines the utility of inviscid numerical approaches in computing supersonic retropropulsion (SRP) flow physics for the swift exploration, design, and future optimization of SRP systems. Comparisons against the steady, inviscid model highlighted in this work rely heavily on the Navier-Stokes results of the Exploration Technology Development Demonstration (ETDD) Program's Supersonic Retropropulsion CFD (ETDD SRP-CFD) working group. Section II describes details of the inviscid computational method exercised in this work, along with descriptions of the experimental and viscous, numerical simulation datasets used for comparison. Section III presents the results of the validation study, examining flow field characteristics and surface pressures for single- and multi-nozzle flows.

2. SRP Flow Features

Figure 2 illustrates relevant physical features of SRP flows. The color scheme for the Mach contours is chosen to aid in comprehension, with white representing sonic conditions, reds representing supersonic conditions, and blues representing subsonic conditions. Complex flow physics result from the retropropulsive jet flowing counter to a supersonic freestream.[19, 20, 29, 43, 44] The subsonic interface region between these opposing flows forces deceleration of the jet, here depicted through a Mach disk. Similarly, the freestream flow experiences a bow shock as it encounters the effective body consisting of the capsule and jet. The interface between the jet and freestream flows is better portrayed in a plot of stagnation temperature (Fig. 3); since stagnation temperature remains constant across shocks and expansions, the freestream and jet flows can be differentiated. Streamlines show the turning of the subsonic flow at the interface. A shear layer forms due to the recirculation region behind the large plume, re-acceleration of the flow occurs through an expansion aft of the shoulder, and the sting then induces an oblique shock. The oblique portion of the primary bow shock experiences a shock reflection at the tunnel wall in the upper section of Fig. 2.

With such rich physics, SRP flows also include viscous effects such as turbulent mixing and boundary layers. Viscous stresses are high in the free shear-layers bounding the jet, and as instabilities in these shear-layers grow, turbulent mixing develops and can dissipate the jet.[45, 46] Accurate eddy-viscosity predictions of free shear-layers remain a challenge for modern turbulence models. Within the nozzle and along the body, boundary-layers are generally thin and inviscid physics tend to dominate these flows. However, prediction
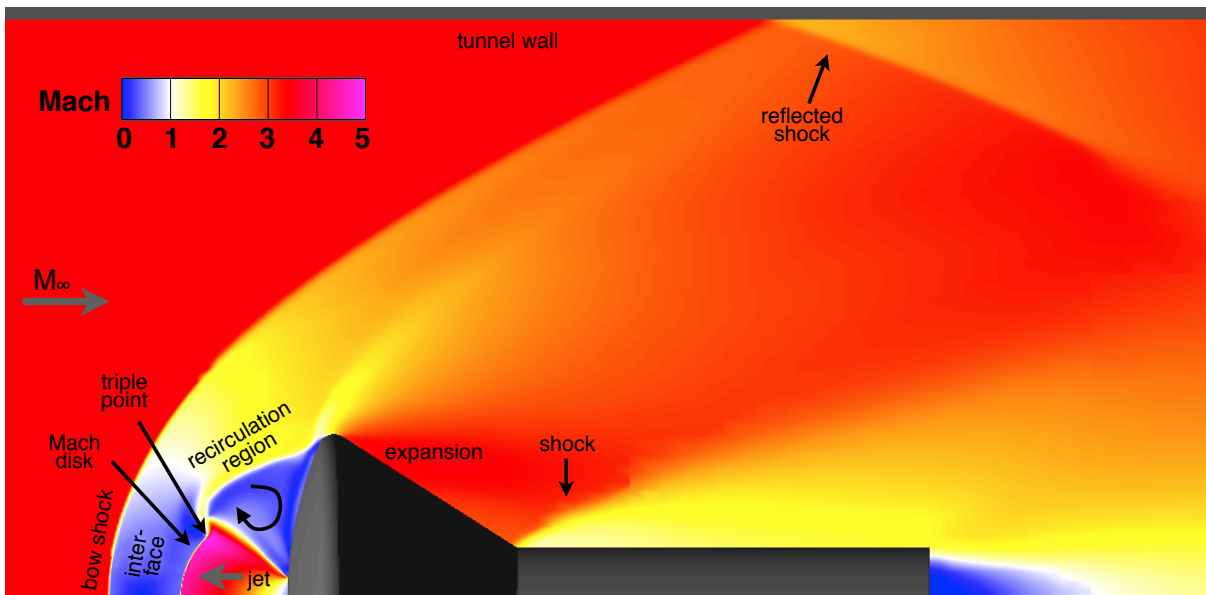

Figure 2. **Mach contours illustrating SRP flow features resulting from an inviscid simulation of the Daso configuration (Sec. IIB.1).**

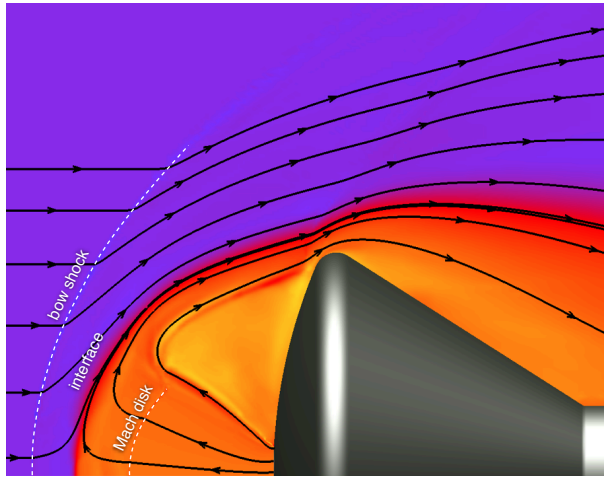American Institute of Aeronautics and Astronautics

Figure 3. Stagnation temperature contours showing interface between violet freestream flow (left to right) and orange jet flow (right to left) for the configuration in Fig 2.

of some characteristics such as strong thermal gradients require viscous calculations. This work compares inviscid solutions against experimental results and viscous numerical solutions to evaluate the utility of inviscid methods for predicting SRP flows.

II.   Approach

The validation studies in this paper employ published experimental SRP wind tunnel data and associated unsteady, viscous simulations results for comparison against the steady, inviscid simulations conducted here. This section describes these viscous methods and experimental datasets, and provides details on the inviscid method and adjoint-based mesh refinement used for the current study.

A.   Computational Method

This study was accomplished using the inviscid simulations and adaptive mesh refinement of NASA's AERO (Adjoint ERor Optimization) package. This section briefly describes the Cartesian-based Euler solver and provides an overview of the adjoint-based mesh refinement module.

This method uses a parallel, multi-level Euler solver on automatically-generated Cartesian meshes with embedded, cut-cell boundaries. The basic package, developed in References 47 and 48, has recently been extended to include an adjoint-based mesh adaptation method to guide cell refinement and control discretization errors present within complex flow fields.[49–51]

The spatial discretization of the Euler equations uses a cell-centered, second-order accurate, upwind finite-volume method. Solid-wall boundaries use a cut-cell approach with weak imposition of the no-flux boundary condition. Steady-state flow solutions are obtained using a five-stage Runge-Kutta scheme with local time stepping, using the flux-vector splitting approach of van Leer and multigrid convergence acceleration.[47, 48, 52–54] The solution algorithm for the adjoint equations utilizes the same parallel, multi-level framework as the base Euler solver.[49, 50]

Widely used for producing aerodynamic databases in support of engineering analysis and design due to its robustness and speed, this inviscid simulation package suits the current preliminary design stage of SRP studies.[55–57] Moreover, this work focuses on simulations with strong and unfamiliar off-body flow features, making it difficult to create appropriate meshes manually. The adjoint-based mesh adaptive approach described here allows automation of the meshing process, and includes information on mesh convergence and discretization error with each simulation.

As simulation geometries and flows become more complex, the ability to create a suitable mesh *a priori* presents an increasing challenge. Parametric and optimization studies amplify this problem by requiring hundreds of potentially unique meshes. We address this need through use of an output-based mesh adaptation method. Following the creation of a coarse starting mesh upon which the initial flow solve is computed, a cell-wise error-estimate is calculated using the method of adjoint-weighted residuals.[49, 58] The mesh is refined

following a "worst things first" approach, and the process repeats until a minimum error or maximum cell count (user-selected) is reached. Mesh sizes for the SRP simulations in this study typically reach approximately 6 million cells. Further details on the adjoint-based refinement method are provided in Refs. 49–51 and 59.

In addition to the steady state runs, numerous unsteady SRP simulations have also been performed in assessing SRP flow physics. The time-accurate flow solver uses a dual-time formulation in which the core parallel multigrid solver is used to efficiently converge an inner pseudo-time iteration.[60,61] Since cut-cells within the domain could place small stability restrictions on the simulations, this formulation uses an unconditionally-stable, implicit scheme allowing timesteps to be chosen based upon physical considerations. Details of the numerical development are in Refs. 62 and 63.

B. Studies Used for Comparison

SRP studies giving both experimental and numerical data are scarce in the literature. Jarvinen and Adams[9] is one such case, and was the subject of the inviscid validation study in Ref. 27, however discrepancies in the experimental geometry and omissions of tunnel stagnation values, when compounded with the poor quality of the Schlieren images, motivates supplemental validation studies.

The current study focuses on two different configurations. The first is a single, central-nozzle model studied in a 2007 experiment[16,43] and used for viscous CFD validation in 2010 by the ETDD SRP-CFD working group.[28] The second is a study of both central and peripheral SRP nozzles performed in the Langley Unitary Plan Wind Tunnel (2010) with a related ongoing ETDD SRP-CFD Navier-Stokes validation study.[28,31,35,37,38,41,42] Comparison against these results affords an investigation of the predictive capabilities of our inviscid approach for the analysis of fundamental SRP flow physics.

1. Experimental Dataset 1: Daso Configuration

The inviscid computational results are compared with data from a wind tunnel study performed by Daso *et al.* in Refs. 43 and 16. These single-nozzle central SRP experiments were performed with the aim of studying the reduced aerothermal loads and wave drag due to the shock wave dispersion caused by the counterflowing jets. Data was taken in the Marshall Space Flight Center's trisonic wind tunnel (MSFC TWT), which has a 21in long test section with a square 14in cross-section. A 2.6% scale model (4in diam) of an Apollo-like capsule (Fig. 4) was tested at Mach 3.48 and Mach 4.0 freestreams with 5 different nozzle designs[a], 5 jet flow rates (with air as the exhaust gas), and angles of attack ranging from $-9°$ to $5°$.[43]

The published experimental data solely consists of flow visualizations from high-quality Schlieren images and heat flux measurements

Figure 4. Tunnel model, from Ref. 43.

- surface pressure measurements were omitted, and only a subset of the tested runs were released and discussed. The ETDD SRP-CFD working group ran a preliminary Navier-Stokes validation study at 0.5 lb_m/s flowrate from the sonic nozzle with 0.5in diameter at a freestream Mach of 3.48 and 0° angle of attack.[28] For the current study, we use the same geometry and flow conditions. The experimental run conditions used in this work are a freestream stagnation pressure and temperature of 44.92psi and 581.38R, respectively, and stagnation jet pressure and temperature of 104.30psi and 479R, respectively.[b]

2. Experimental Dataset 2: Langley UPWT Configuration

An SRP experiment, performed in July 2010 in the Langley Research Center Unitary Plan Wind Tunnel (LaRC UPWT), collected data on single- and multi-nozzle SRP flows. Test setup along with preliminary experimental results are described in Refs. 41 and 42, and detailed data and uncertainty analysis are ongoing.[42] Configurations comprising 0-, 1-, 3-, and 4-jet models were tested at freestream Mach numbers

---

[a]The nozzle contours were created with an in-house design code utilizing the method of characteristics with a boundary layer displacement thickness correction.[43]

[b]References 43 and 16 gave slightly different conditions for freestream stagnation values; the values indicated in Reference 16 are used here.

of 2.4, 3.5, and 4.6 at angles of attack spanning $-8°$ to $20°$ and C_T values ranging from 0.5 to 3. The test model consisted of a 5in diameter $70°$ sphere-cone forebody accommodating up to four 4:1 area ratio nozzles (placed on the centerline and at halfway along the forebody radius as seen in Fig. 5), followed by a cylindrical aftbody, bringing the model length to 10in. in the approximately square 4ft test section. Instrumentation included 167 static surface pressure ports on the model forebody and aftbody sampling over 2.5s at 10Hz, 7 Kulite pressure transducers mounted on the forebody to measure both time-averaged and unsteady surface pressures, and high-speed Schlieren images recorded at approximately 1000 frames per second.

3. Viscous CFD Datasets

Numerical validation is currently a focus for the ETDD SRP-CFD working group, based primarily on the DPLR, OVERFLOW, and FUN3D CFD codes. A brief description of each is given in this section. Grid sizes for the Navier-Stokes SRP simulations in this study range from 28 million (FUN3D) to 55 million grid points (OVERFLOW and FUN3D). Additional information on design order and grid sensitivities can be found in Ref. 38.

Figure 5. Model configurations, with x in freestream direction, z to tunnel ceiling, and y spanwise.

The Data Parallel Line Relaxation (DPLR) code[64] is a parallel, cell-centered structured multi-block, finite-volume code which solves the Reynolds-Averaged Navier-Stokes (RANS) equations. Based on information given in Reference 28, DPLR was run time-implicit with first-order temporal accuracy and a perfect gas assumption. Euler fluxes were computed using third-order accurate modified Steger-Warming flux vector splitting, and second-order accurate viscous fluxes were calculated. Vorticity-based SST (Shear-Stress Transport) was implemented as the turbulence model with no compressibility correction.

OVERFLOW 2 (OVERset grid FLOW solver)[65–68] is an implicit RANS flow solver utilizing node-centered structured overset grids.[28] The HLLE++ numerical flux function was used for spatial terms, and the temporal terms were calculated using the Symmetric Successive Over Relaxation (SSOR) algorithm with Newton subiterations. All viscous terms were included, and several turbulence models were employed, including a strain-based SST method with and without compressibility corrections and the Spalart-Allmaras method for the Daso case, the RANS SST model subject to Wilcox's realizability constraint for the quad-nozzle LaRC UPWT case, and a SST-DES hybrid model with the realizability constraint for the single- and tri-nozzle LaRC UPWT cases.[28, 31, 38, 40] Overall, the chosen scheme was formally second-order accurate in space and time.

The Fully Unstructured Navier-Stokes Three-Dimensional (FUN3D) code[69, 70] is a node-based finite-volume flow solver. For the Daso study, the Edwards' Low-Dissipation Flux Splitting Scheme (LDFSS) flux function was employed to solve the compressible RANS equations coupled to Menter's (strain-based) SST turbulence model; for the LaRC UPWT study, a vorticity-based SST turbulence model was used. Solutions in both cases were computed by driving a second-order accurate spatial residual to steady-state using a point-implicit iterative method.[28, 40]

III.   Results and Discussion

Examination of the inviscid numerical scheme's ability to predict complex SRP flows is accomplished in two parts. Comparisons against the the single central-nozzle Daso experiment and related results from Navier-Stokes codes are described in Section IIIA. Then, both single- and multi-nozzle SRP flows are investigated utilizing the Langley experimental data and related Navier-Stokes code comparisons in Section IIIB, which also includes an unsteady inviscid analysis of SRP flows.

A.   Daso Configuration

The experimental configuration and conditions reported in Refs. 43 and 16 (described in Section IIB.1) provide a basis for evaluating numerical results. This section compares inviscid numerical results with both
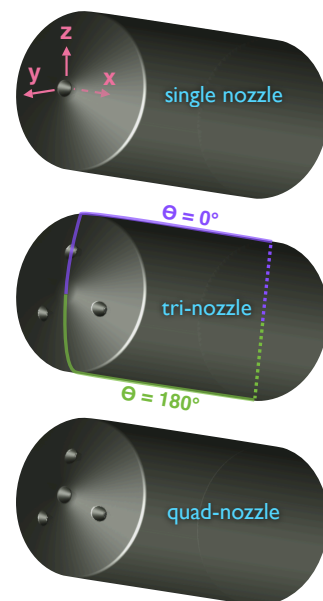
American Institute of Aeronautics and Astronautics

experimental and Navier-Stokes numerical solutions, with analysis focuses on the freestream Mach 3.48 case at 0° angle of attack using boundary conditions for a 0.50lb_m/s (C_T of 0.4) jet flow rate.

The Daso configuration represents one of the first validation cases completed by the ETDD SRP-CFD working group.[28, 31] The geometry was created based on the 4in diameter Apollo capsule and central 0.5in.-diameter sonic nozzle described in Sec.IIB.1, but different sting lengths were modeled between each viscous code, and nozzle geometries differed slightly: the OVERFLOW and inviscid simulations applied boundary conditions at the converging section of the nozzle, while the FUN3D and DPLR simulations included a plenum section. Tunnel walls were included in the inviscid simulations, however the viscous simulations were all performed in free air. Domain sizes varied significantly among the viscous solvers.

The inviscid simulation was run using the adjoint-based mesh refinement method described in Sec. IIA. The initial mesh of 30,000 cells was refined in a series of automated adaptation cycles, resulting in a final mesh of 3.8 million cells (Fig. 6). Figure 7 examines convergence of the functional and its error-estimate, giving a strong indication of mesh convergence in the simulation. The frame at the left shows this directly with changes in the functional[c] decreasing as the mesh is refined. The central frame illustrates convergence of the adjoint-based estimate of the error in the functional. After the first mesh refinement, this estimate decreases steadily, indicating that the mesh refinement is systematically eliminating discretization error in the computational domain. The frame on the right shows the convergence history of drag force, depicting a slight "unsteadiness," or noise due to incomplete convergence of the residual in the last adapt cycle.
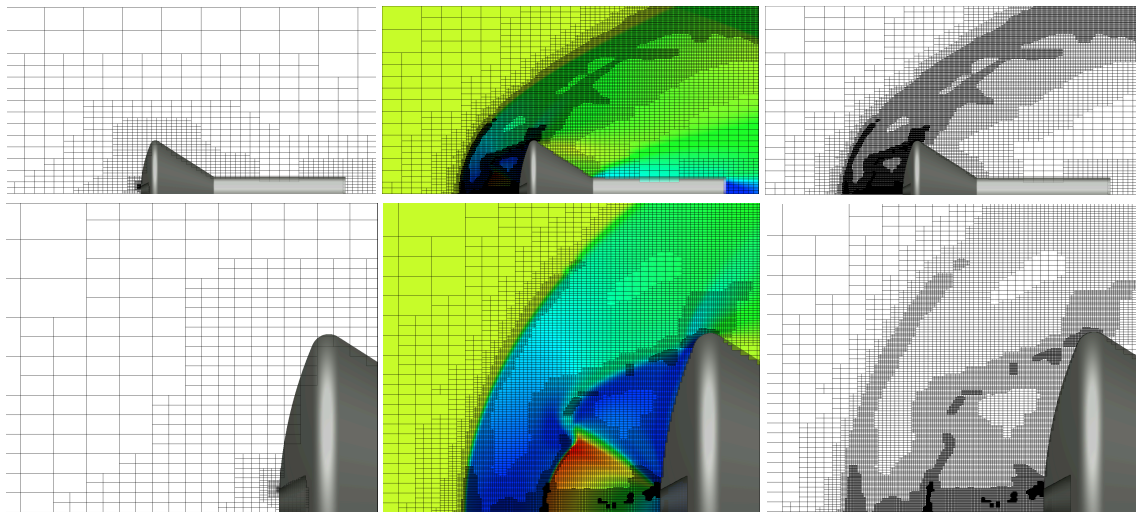

Figure 6. Initial (left) and final (right) grids for the inviscid simulation, with flow solution on finest grid (center).
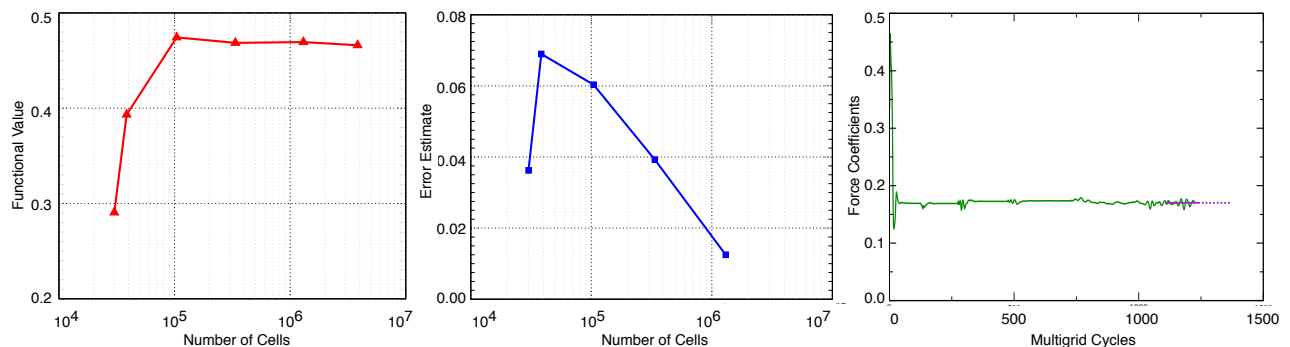

Figure 7. Mesh convergence of the functional, error-estimate, and force coefficient (with iterative average on last adapt cycle).

---

[c]The functional is based on body drag and lift forces, in addition to pressures along a sensor at the tunnel wall to locate the bow shock away from the body.

American Institute of Aeronautics and Astronautics

Figure 8 compares numerical Mach contours from the inviscid calculation to an experimental Schlieren image from Ref. 43[d]. The numerical method captures the bow shock and Mach disk locations in agreement with the experimental results, and similar plume wake regions can clearly be seen in both images. The jet boundary and bow shock shape of the inviscid solution appear consistent with the experimental flow results. With no quantitative experimental data available, all further analysis consists of code-to-code comparisons.

The Mach contours in Fig. 9 give a qualitative comparison between the inviscid results and data from viscous solutions obtained with FUN3D, OVERFLOW, and DPLR; Fig. 10 illustrates flow feature locations for each numerical solution by plotting Mach number along an axial cut through the center of the nozzle. As expected, jet expansion in the plume is almost identical across the simulations despite differences in plenum geometry. The FUN3D plume solution reaches slightly lower Mach numbers, but places the Mach disk in agreement with OVERFLOW and DPLR. The plume in the inviscid solution appears slightly larger, with a Mach disk location only slightly farther from the nozzle exit as compared to FUN3D and visibly farther as compared to OVERFLOW. The DPLR solution showed a degree of plume unsteadiness.[28] Subsonic flow in the interface region is extremely similar for the inviscid, OVERFLOW and FUN3D solutions. Bow shock locations show some variability: the inviscid and FUN3D solutions are extremely similar and consistent with the experimental data, and the OVERFLOW and DPLR predictions fall on either side of this average.

Figure 8. Numerical Mach contours (top) versus experimental Schlieren results (bottom).

Differences in the plume wake flow and shear layer are apparent in Fig. 9. OVERFLOW, FUN3D and the inviscid model solutions in the plume wake region appear increasingly diffuse due to different levels of dissipation. Simulations with FUN3D and OVERFLOW predict steady flow in that region, while the DPLR simulation predicts unsteadiness, and inviscid modeling convergence indicates slight unsteadiness with no
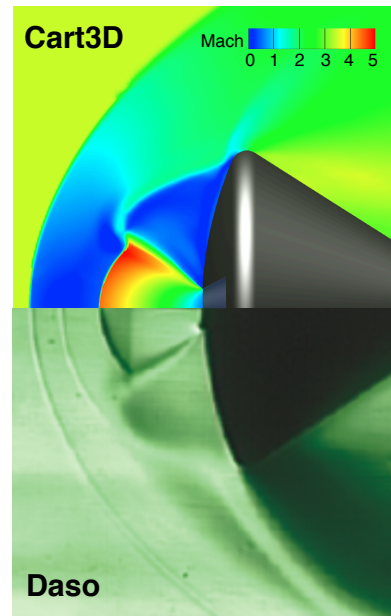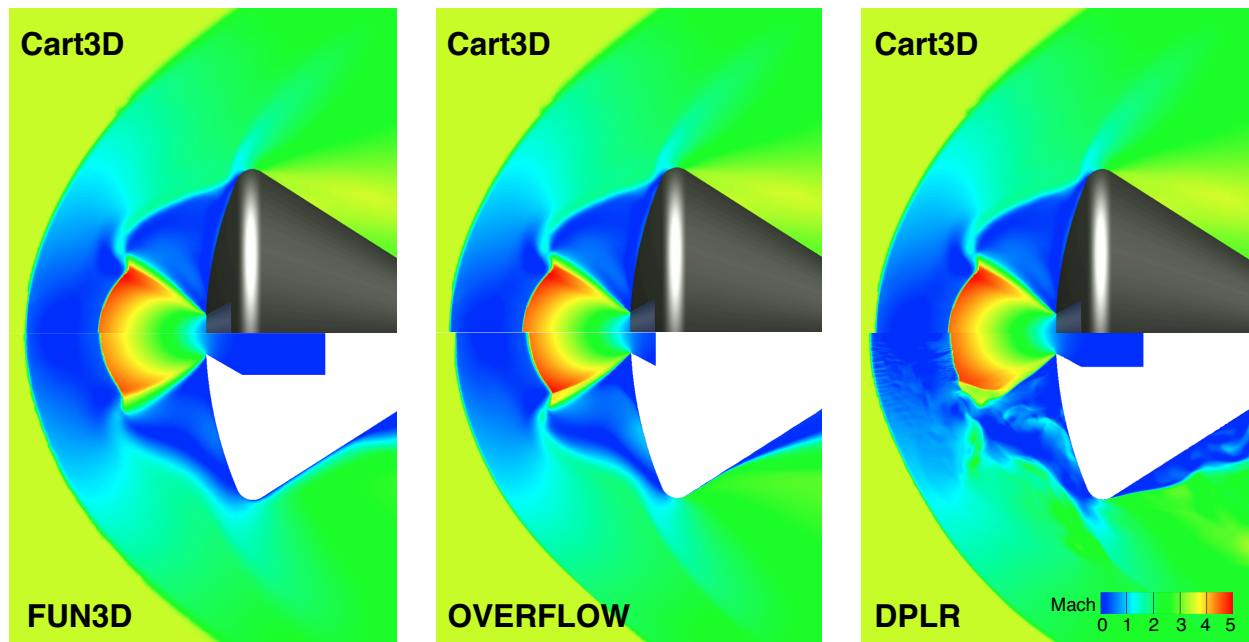

Figure 9. Mach contour comparisons between simulations using the Cartesian, inviscid method and (left to right) FUN3D, OVERFLOW, and DPLR.

---

[d]Images aligned as closely as possible in spite of geometry slices not matching in both horizontal and vertical directions, likely due to the camera angle in the experiment.
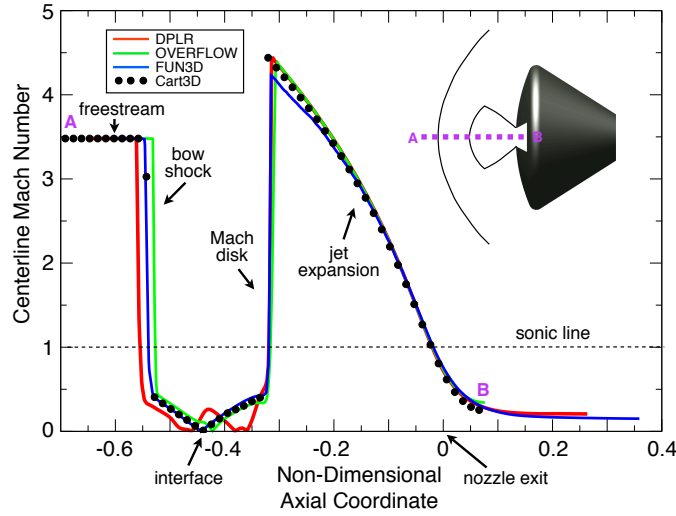
Figure 10. Mach number along a centerline cut (center of the nozzle) showing SRP flow feature locations.
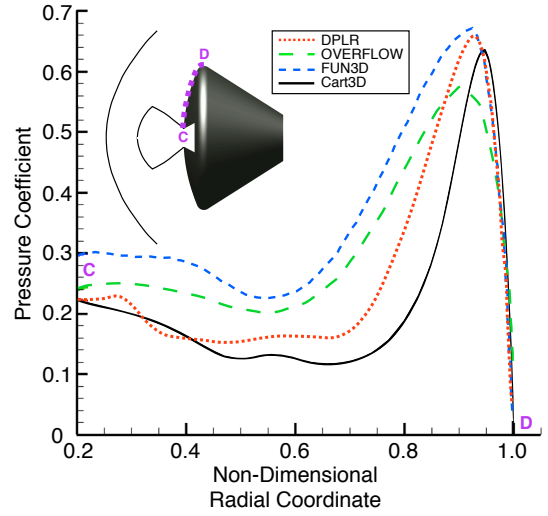

Figure 11. Pressure coefficient on the capsule face.

zero residuals in the shear layers. This is consistent with experimental reports of slight unsteadiness in forebody sensor readings.[16,43]

All 4 solutions exhibit a compression at the shoulder. As illustrated in Fig. 11, capsule face pressures are extremely low due to the recirculating plume wake flow, and only increase near the shoulder at the shear layer impingement area. Following the flow through the expansion at the capsule shoulder, the viscous simulations show a thickening of the boundary layer as the static pressure drops. The flow separation locations differ depending on grid resolutions and dissipation levels.[28] As expected, no separation is triggered by the smooth geometry in the inviscid simulation; however, since pressures downstream of the shoulder drops radically in these blunt body flows, the difference in the aft flowfields have little effect on force coefficients of the model.

Variations in C_P (Fig. 11) amongst the three viscous simulations performed by the ETDD SRP-CFD group and by the inviscid method applied for this study attest to the complexity of modeling SRP flows. We expand our study to multi-nozzle flows in the next section, using the pressure, frequency, and image-based results of the Langley UPWT experiment as a basis.

B.   LaRC UPWT Configuration

Inviscid solutions of single- and multi-nozzle SRP flowfields and body pressure coefficients are compared against viscous numerical solutions (DPLR, OVERFLOW, and FUN3D) and wind tunnel data for the LaRC UPWT configuration. The configuration and flow conditions for the 7 cases examined in this section are indicated in Table 1, all at low C_T and a freestream Mach number of 4.6. Section IIIB.1 analyzes both steady and unsteady inviscid solutions as compared to experimental and viscous numerical results, examining in depth the oscillatory behavior of a single-nozzle case and establishing the utility of a steady, inviscid code to predict SRP flow physics. Sections IIIB.2-4 then present each of the single-nozzle, tri-nozzle, and quad-nozzle cases, respectively, reporting and comparing steady inviscid, unsteady viscous, and raw[e] experimental data.

Table 1.   Condition matrix for SRP analysis.

run	# nozzles	M_∞	C_T	α
165	1	4.6	2	0°, 12°, 20°
262	3	4.6	3	0°, 16°
307	4	4.6	2	0°, 20°

---

[e]Without wind tunnel corrections, errors, or uncertainty estimates, which are not yet published.
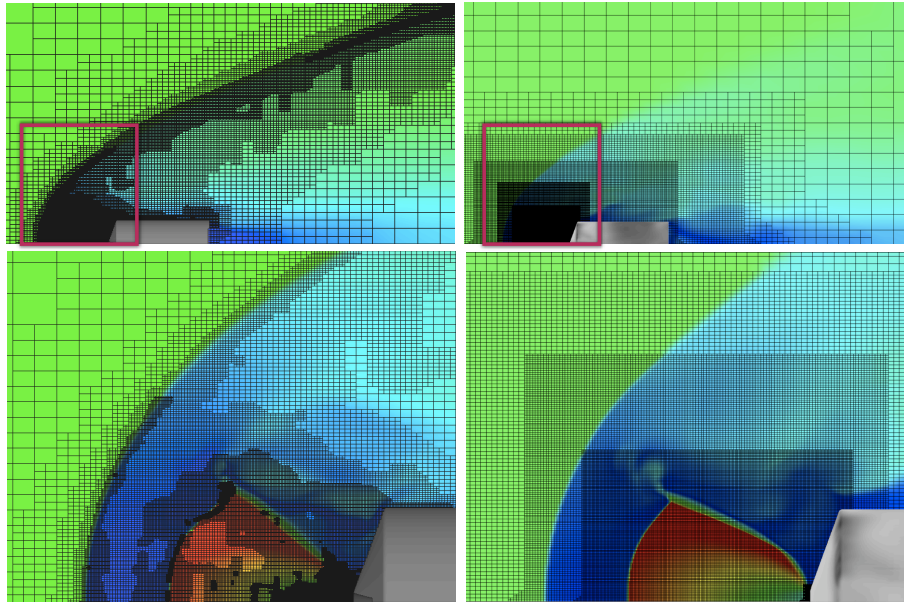
Figure 12. Adjoint-based (left) mesh for steady, inviscid calculation vs. (right) mesh for unsteady, inviscid calculation.

1. Steady vs. Time Accurate Simulations

The lower computational cost of steady, inviscid modeling is appealing for studies requiring myriad runs such as parametric studies and optimization problems which are inevitable during the development of SRP technology. In order to ascertain the modeling error in using a steady solver for predicting unsteady flows, here we analyze SRP solutions resulting from both steady and unsteady inviscid simulations. We focus on the LaRC UPWT single-nozzle 0° angle of attack case (run 165 in Table 1) since this case was used as a benchmark by the ETDD SRP-CFD group for an unsteady frequency analysis.[38]

The steady solution utilized the automatic, adjoint-based mesh refinement method described in Section IIA and demonstrated in Fig. 7. The final solution was solved on a 6.5 million grid point mesh (left column of Fig. 12) resulting from 6 mesh adaptive cycles driving down the discretization error in the computational domain, and the total solution time was 25 core hours[f].

The full unsteady simulations was run using a time-accurate version of the same Cartesian Euler solver, described in Sec. IIA. Manual generation of a mesh suitable for the unsteady calculation was guided by the adjoint-based grid. A mesh refinement study for the unsteady solution resulted in a final grid size of 9 million cells (right column of Fig. 12). Time convergence was also established on each unsteady grid, resulting in a non-dimensional timestep of 0.002 which corresponds to a physical timestep of $12.40\mu s$. The time accurate solution required approximately 34 times more computational effort than the steady-state run.

Figure 13 illustrates the periodic unsteady, inviscid solution as sampled in four snapshots evenly spaced over a single period. In this two-dimensional centerline slice, a vortex is shed off the outer edge of the plume at (a), propagating downstream at (b) and (c) towards the forebody. The pressure disturbance at the nozzle exit (d) affects the plume expansion, enabling pressure disturbances to propagate back upstream as the jet boundary fluctuates as shown with (e)-(h). This feedback loop results in a strongly periodic three-dimensional flow,
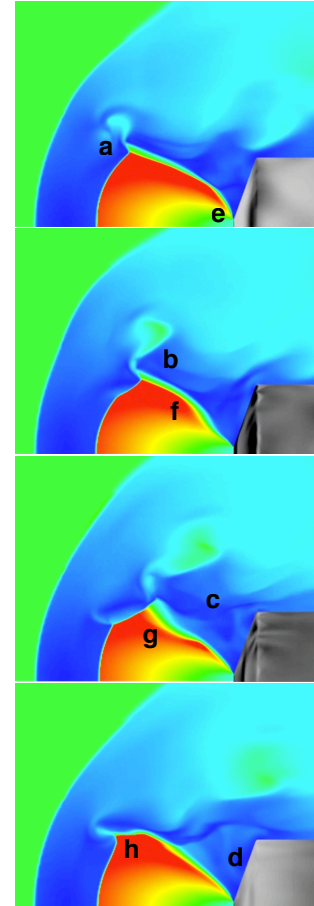

Figure 13. Mach cont[...] snapshots over a single [...] riod of oscillation.

---

[f]Core hours based on Intel Xeon X5670 CPU at 2.9GHz.

American Institute of Aeronautics and Astronautics

Run 165 Jets 1 Mach 4.6 Re 1.5e
Alpha 0 deg Roll 180 deg
PTJ 598.9 psia TTJ 162.4 deg
T 1.97 PTJ/PINF 7724.3 TTJ/TINF
Recorded at 6245 fps

Mach
0 2 4 6 8 10

time step: 0.002
nsional time elapsed: 4.448

3 4 5 6 7 8 9 10

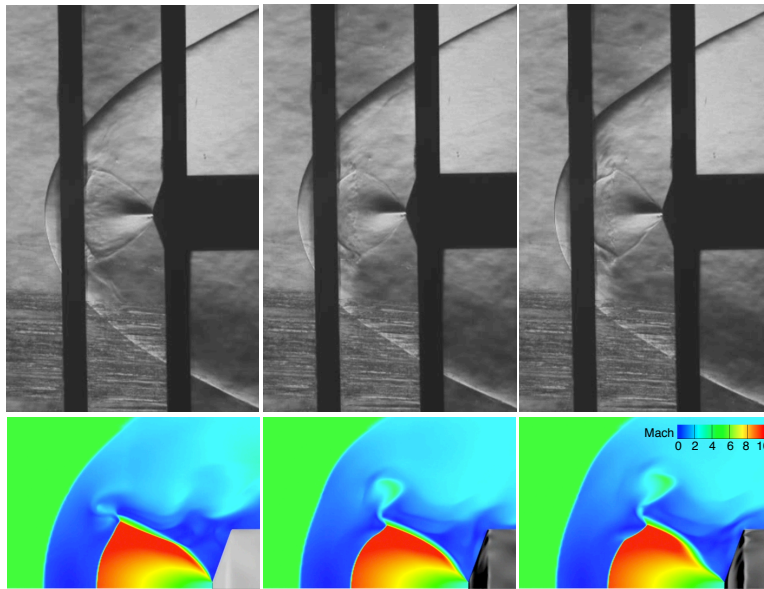**Figure 14. Snapshots of unsteady flow, c_____ jet boundary shape in experimental Schlieren images and inviscid solution (bottom).**

experiencing oscillations in the triple p____ __n and the jet boundary due to this inviscid vortex ring shedding mechanism, as described. The bow shock and Mach disk show some fluctuations but maintain their basic positions as seen when comparing the images of Fig. 13. The reduced frequency of this shedding mechanism is computed to be 13 based on wave propagation speeds in different domains of the flow, translating to 2.1kHz based on the relevant time and length scales of the problem.

Figure 14 illustrates similarities in plume shapes and jet boundary locations, comparing snapshots of the flowfield from the inviscid, time-accurate solution (bottom) to instantaneous experimental Schlieren images (top). By computing a Fast Fourier Transform (FFT) of the axial force, the dominant frequency of the oscillation was measured at 2.10_____ nviscid, unsteady simulation, falling near the middle of the experimental reported range of 1.___ ___nd corresponding well with the proposed inviscid mechanism. The experimental frequency resu___ ___ished in Ref. 42 through post-processing of data from the forebody pressure transducers to ___ ___ean-square averaged fluctuations and a power spectral density function.[40] The experimental fre___ ___s correlated with the vertical sensor location on the forebody, and is attributed to a possible ___ ___ in the tunnel flow at a 0° angle of attack configuration.[42] Frequency and timestep comparis___ ___viscid, viscous, and experimental data are detailed in Table 2. Ref. 38 reports OVERFLOW and ___ ___ion frequencies for this case at 2.1kHz as well, computed by measuring the steps per cycle of t___ ___ The DPLR solution frequency was calculated through a FFT of sampled pressure at several fo___ ___ns, beginning with a frequency of 1.8kHz, which tailed off as the oscillation in the solution eve___ ___ed.[38] Overall, analysis of this benchmark SRP case resulted in excellent agreement in frequen___ ___ by the inviscid model, viscous simulations, and experiment.

T____ ____lation frequency comparison.

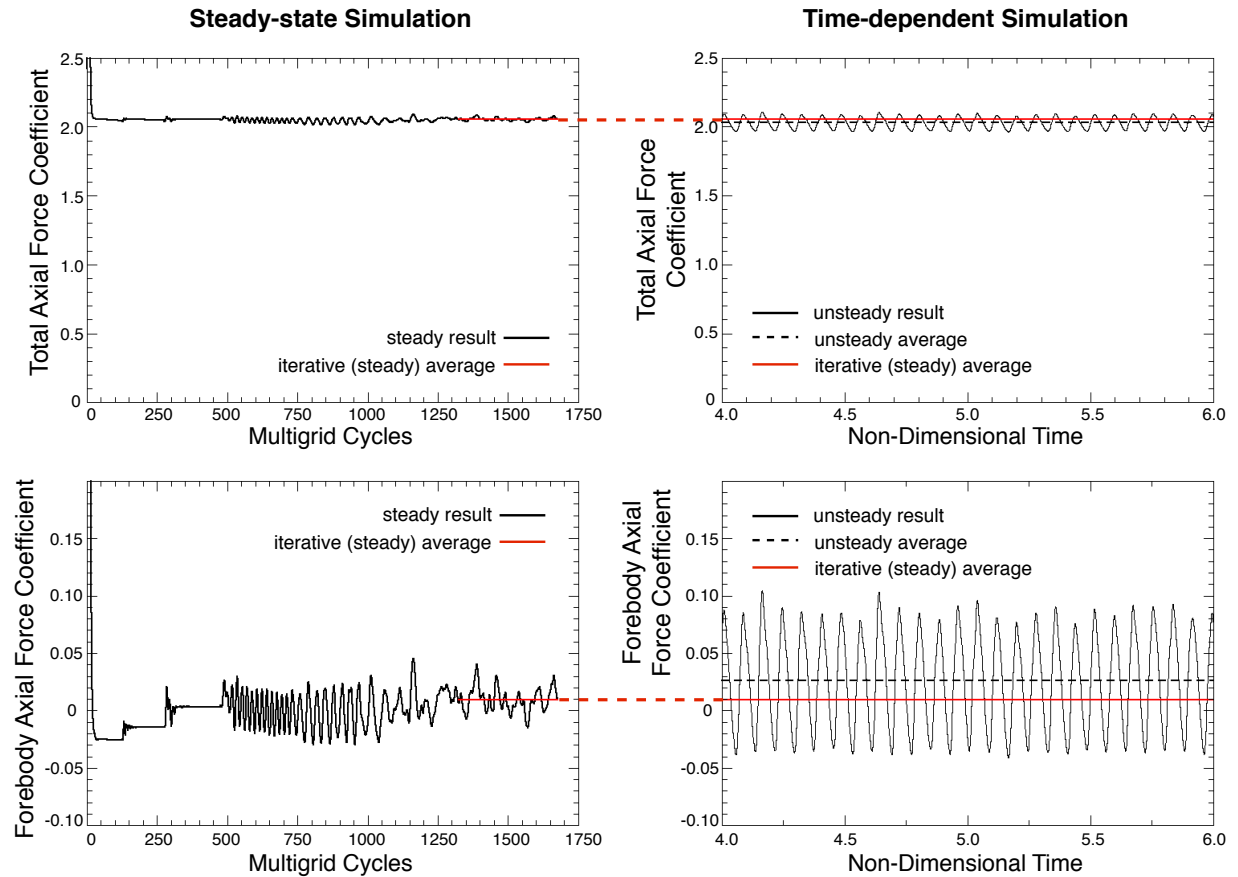|	___ints	timestep (μs)	frequency (kHz)
experimen___		25^g	1.7-2.3
DPLR	___00	0.324	1.8→0
OVERFLO___	___00	0.685	2.1
FUN3D	___,000,000	2.36	2.1
inviscid	9,000,000	12.40	2.1

[g]Based on a 40kHz sampling rate.

Figure 15. Iterative force averages for the steady inviscid simulation (left) compared to unsteady force oscillation averages (right).

Having accurately captured the dominant unsteady, inviscid mechanism and frequency, we can examine modeling errors accrued through use of a steady, inviscid solution. In this case, unsteadiness manifests itself as unsatisfied residuals. Figure 15 depicts convergence histories of forces for the steady, inviscid method as a function of multigrid cycles in the images to the left, and force results for the unsteady, inviscid method on the right. Total axial force coefficient and forebody axial force coefficient are plotted in the upper and lower figures, respectively, with the force scales identical in each row of images to facilitate comparison between the two solutions. The iterative averages for the forces modeled using the steady solution can be compared to the unsteady force oscillation averages in Table 3, suggesting the feasibility of estimating these type of flows with a steady, inviscid modeling tool. The close agreement between the time-averaged coefficients and the steady-state results supports the use of steady, inviscid modeling to reasonably predict these flows, especially given the wide disparity in computational cost (Table 3). In the remainder of this work, we compare results for the steady, inviscid model to data from the experiment and time-accurate viscous simulations.

Table 3. blargety blarg blarg. both inviscid method.

	CPU time	# grid points	$C_{A,total}$	$C_{A,forebody}$
unsteady time average	844 core hours	9,000,000	2.03053	0.026083
steady iterative average	25 core hours	6,500,000	2.05435	0.00931584
Δ			0.02382	0.01676

American Institute of Aeronautics and Astronautics

2. Central Single-Nozzle Configuration

Figure 16 shows centerline pitch-plane Mach contour comparisons for the single nozzle case (Table 1) at different angles of attack. Concentrating first on the 0° case, we note typical SRP flow features described in Fig. 2 such as the Mach disk terminating the supersonic jet flow, plume triple point, subsonic region between the Mach disk and offset bow shock, and subsonic flow between the plume and forebody. All four simulations predict close shock standoff distances, plume sizes, and Mach disk shapes. The inviscid and DPLR solutions show extremely close agreement, with similar jet expansions, jet boundary shapes, and triple point locations. As established in Section IIIB.1, this case experiences slight unsteadiness associated with an inviscid vortex shedding from the triple point region. Since the images in Fig. 16 are instantaneous snapshots, the differences in the OVERFLOW solution may be an artifact of timeslice choice.
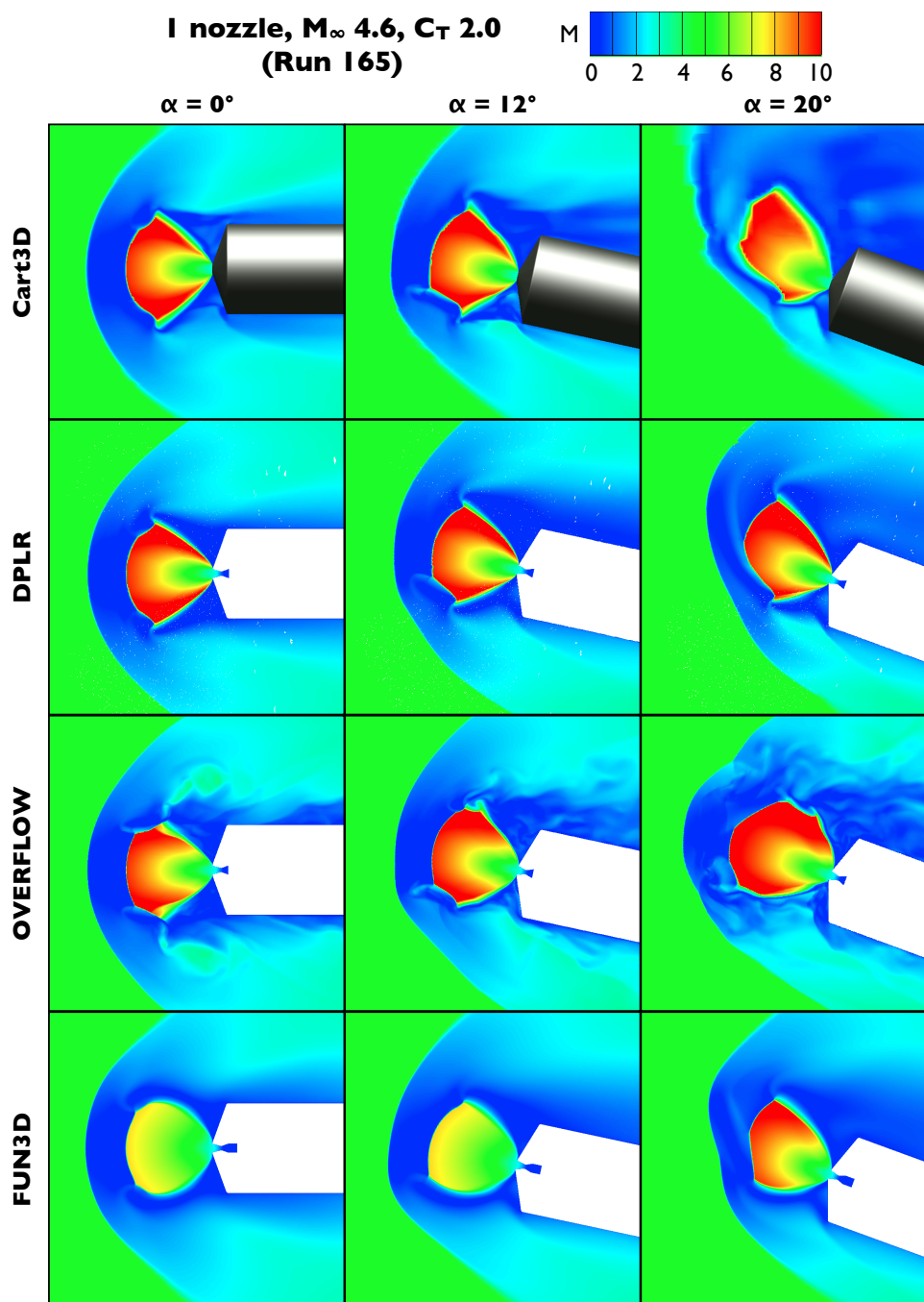

Figure 16. Instantaneous centerline pitch-plane Mach contour comparisons for the single-nozzle case.

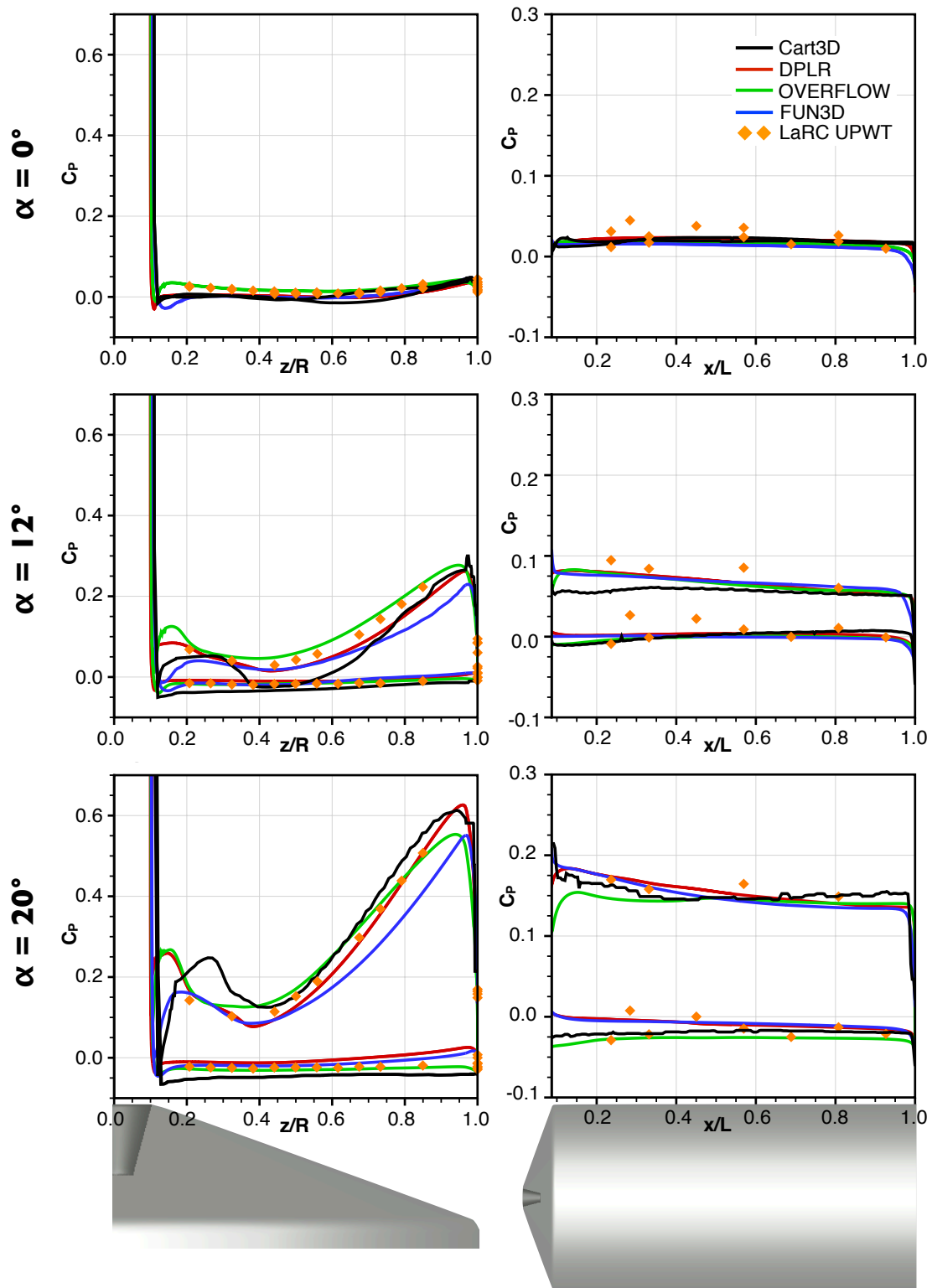American Institute of Aeronautics and Astronautics

Figure 17. Pressure coefficient comparisons over the forebody and sidebody for the single-nozzle case.

The 12° case, shown in the middle column of Fig. 16, shows similarities between the plume shapes resulting from the inviscid and DPLR simulations, with the leeward portion of the plume maintaining a structure similar to the 0° case. In addition, the windward side of the plume is deformed by the oncoming freestream flow in both cases, resulting in a bow shock shift in that region. Compared to the 0° case, the unsteady simulations capture more intense vortex shedding from the windward triple point.[40] The OVERFLOW solution captures a windward triple point structure similar to the inviscid and DPLR simulation results. All four solutions experience larger subsonic regions on the leeward side of the plume as compared to the 0° case, which affects the leeward shoulder and subsequent pressures.

The 20° case shows agreement between the inviscid, DPLR, and FUN3D simulations, with a resulting elongated plume and similar asymmetric plume termination structures. As with the 12° case, the leeward portion of the plume maintains a similar structure to the baseline 0° symmetric plume case while the windward plume structure is substantially altered. All the unsteady solutions demonstrate increased unsteady behavior for this case, with no clear periodicity as experienced at the lower angles of attack.[40] The Mach contours of Fig. 16 suggest that all four solutions capture the deformation of the Mach disk and bow shock.

Figure 17 illustrates C_P data over the forebody (left column) and the sidebody starting at the shoulder (right column) for the central single-nozzle case at several angles of attack, with distances non-dimensionalized by the capsule radius and length, respectively. The numerical results are represented by the solid lines; DPLR, OVERFLOW, and FUN3D solutions are time-averaged, and the inviscid solution is an average over several iterations. Wind tunnel results are given by the symbols and represent raw experimental data generated from the static pressure ports on the forebody and aftbody of the model. Data is given for the $\theta = 0°$ and 180° cuts as depicted in Fig. 5. For the single-nozzle case, this results in a pressure spike at the low radial locations as the cut passes through the plume at the nozzle exit as seen in the forebody C_P plots in Fig. 17. The numerical solutions and experiment all show excellent agreement in the $\alpha = 0°$ case, exhibiting low pressures over the majority of the body. The 12° and 20° cases experience increasingly higher pressures at the windward shoulder due to shear layer impingement in that region. All four numerical solutions capture the basic trends exhibited by the tunnel data, but some differences are apparent. For example, on the forebody in the 20° case, FUN3D and OVERFLOW predict a lower shoulder pressure, the FUN3D solution exhibits a lower magnitude pressure peak at the nozzle exit as compared to the other numerical solutions, and the inviscid method captures a similar pressure peak magnitude to DPLR and OVERFLOW, but slightly farther from the nozzle exit. The sidebody pressure data experience larger variations with increasing α, with OVERFLOW and the inviscid solution predicting lower pressures near the shoulder at high angles of attack.

3. Peripheral Tri-Nozzle Configuration

The left half of Fig. 18 shows centerline pitch-plane Mach contour comparisons between the four simulations for the peripheral tri-nozzle case (Table 1) at various angles of attack. This configuration consists of three equally-spaced nozzles located at half of the forebody radius, as illustrated in Fig. 5. The centerline cut captures a portion of the lower jets in all four images. For the 0° case, the OVERFLOW and inviscid solutions appear to exhibit both unsteady bow shocks and unsteady flow in the interface region behind the bow shock, while the DPLR and FUN3D simulations capture unsteady behavior in the interface region.[40] The plume shapes, sizes, and expansions differ for each code, with the DPLR solution exhibiting the smallest plume structures and the OVERFLOW and inviscid simulations producing the largest plumes with similar triple point and jet boundary shapes, albeit with different levels of expansion. The four solutions exhibit varying signs of unsteady behavior due to the interactions between the plumes; the residual convergence history in the inviscid solution suggests an unsteady solution, the FUN3D simulation exhibits small oscillation amplitudes, and both the OVERFLOW and DPLR simulations predict highly unsteady flows.[40]

For the 16° case, all four simulations predict lengthened plumes as compared to the 0° case. The inviscid solution in Fig. 18 experiences similar bow shock location, shape, and jet expansion and size as compared to the DPLR and FUN3D simulations. The inviscid solution residuals suggest the likelihood of unsteadiness, which is corroborated by the experimental wind tunnel results and the unsteady numerical solutions.

Similar to Fig. 17, Fig. 19 depicts C_P over the forebody and sidebody tri-nozzle configuration. As seen in the forebody plots (left), the $\theta = 0°$ centerline cut passes through one of the three jets, resulting in the expected pressure spike. Concentrating first on the 0° case, pressures at the forebody center are notably higher for this tri-nozzle configuration as compared to the single-nozzle 0° case. The OVERFLOW and DPLR solutions predict the highest nose pressures and nozzle exit pressure peaks, agreeing with the experimental data, while the inviscid method predicts the lowest. The clean (no-nozzle) half of the tri-nozzle forebody
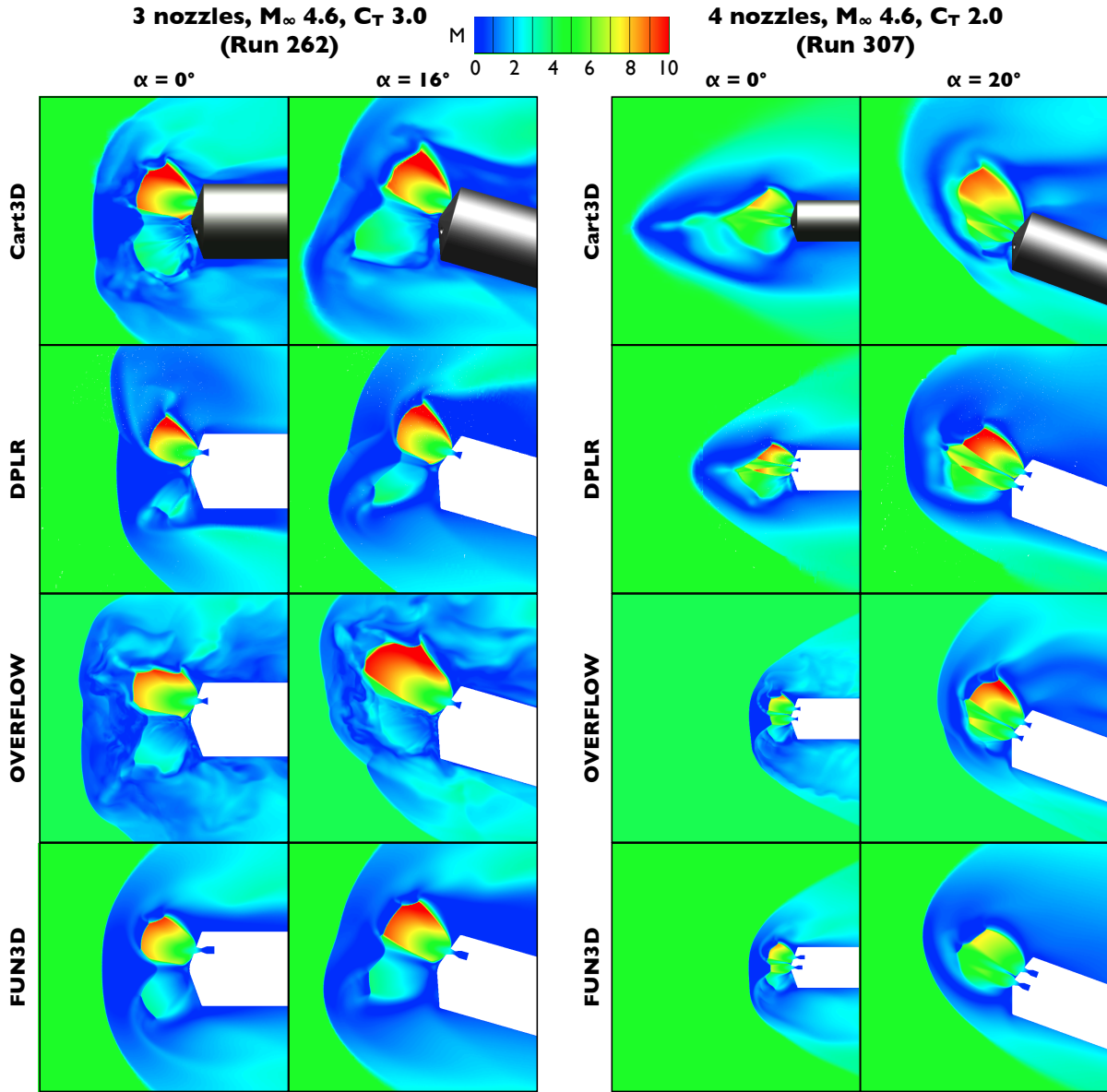
Figure 18. Instantaneous centerline pitch-plane Mach contour comparisons for the tri- and quad-nozzle cases.

is predicted to be a low pressure region, although the OVERFLOW simulation exhibits distinctly higher pressures in that area. The 16° case experiences higher shoulder pressures on the clean half of the forebody (windward side). The experiment and all the simulations capture this trend, with the OVERFLOW solution overpredicting and the inviscid method underpredicting as compared to the average.

4. Peripheral Quad-Nozzle Configuration

Results for the peripheral quad-nozzle case are illustrated in the right half of Fig. 18, which shows centerline pitch-plane Mach contour comparisons between the four simulations at various angles of attack. As shown in Fig. 5, the 4-nozzle configuration is a synthesis of the single-central and tri-peripheral configurations. For the 0° case, the numerical solutions exhibit two different solution types. The inviscid and DPLR simulations experience elongated plume structures with bow shocks extending upstream, as compared to the OVERFLOW and FUN3D solutions which predict blunt distinct plumes and a resulting bow shock located closer to the body.

American Institute of Aeronautics and Astronautics

3 nozzles, M$_\infty$ 4.6, C$_T$ 3.0
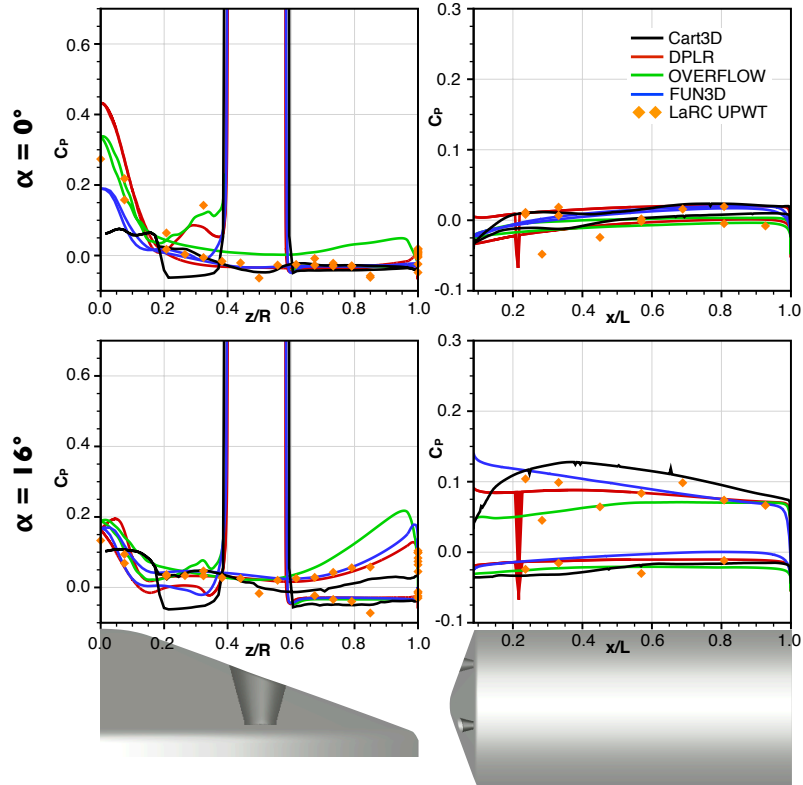**(Run 262)**

Figure 19. Pressure coefficient comparisons over the forebody and sidebody for the tri-nozzle case.

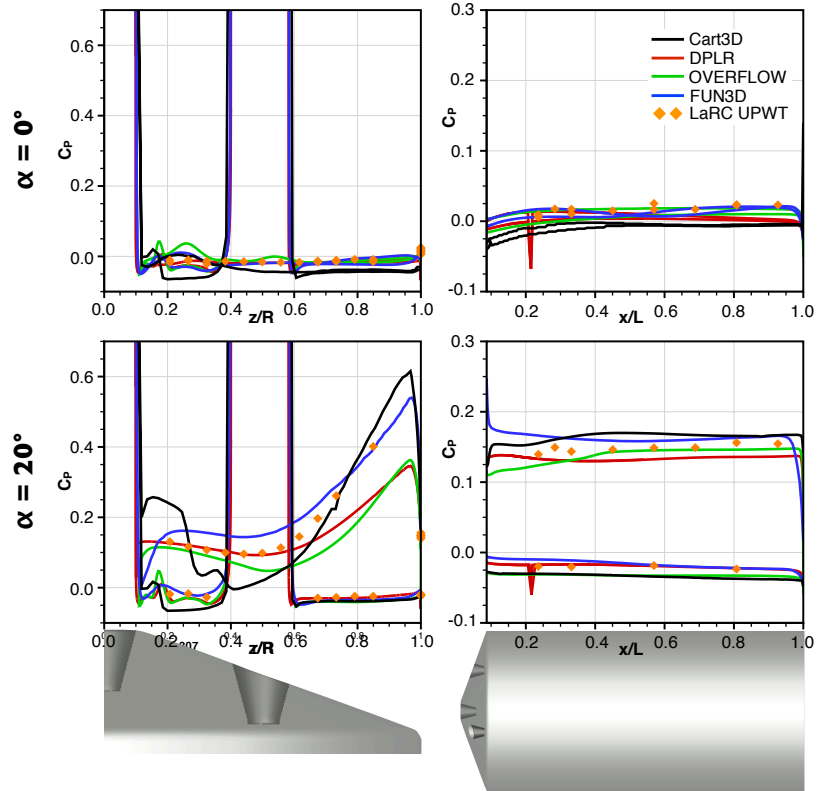**4 nozzles, M$_\infty$ 4.6, C$_T$ 2.0**
(Run 307)

Figure 20. Pressure coefficient comparisons over the forebody and sidebody for the quad-nozzle case.

The 20° case is portrayed in the right column of Fig. 18. All four solutions exhibit similar plume structures, resembling the DPLR and inviscid solutions in the 0° case, capturing slightly elongated plumes, a thin smaller central jet, and coalescing plumes. The plume expansion is seen to vary, with the FUN3D and DPLR simulations predicting the lowest and highest jet Mach numbers, respectively. The experimental results indicate a highly unsteady flow.[40] DPLR and FUN3D simulations reached steady solutions, residuals in the inviscid solution suggest a slight unsteadiness, and the OVERFLOW simulation never reached a steady solution.[40]

C_P results are illustrated in Fig. 20 for the quad-nozzle configuration. The forebody plots depict the pressure rise due to the $\theta = 0°$ slice cutting through both the central nozzle and the upper peripheral nozzle. For the $\alpha = 0°$ case all the simulations predict low pressures over the entire face. The pressure between the two nozzles is slightly overpredicted by the OVERFLOW simulation and underpredicted in the inviscid solution. The inviscid model also predicts a slightly lower pressure at both shoulders as compared to the other simulations. At 20°, there is some variance in agreement. The windward shoulder pressures increase dramatically, with the inviscid and OVERFLOW simulations trending with the experimental data and predicting the largest pressures. Side body pressures are fairly constant, though asymmetric, especially in the 20° case. The four numerical solutions predict a range of pressures at each radial location, and this spread increases with angle of attack.

IV.   Conclusion

This work represents an introductory step in developing the capability of steady, inviscid models for the design of SRP systems. Based on comparison against viscous time-accurate solutions and experimental data, single- and multi-nozzle retropropulsive inviscid flow solutions were shown to capture salient SRP flow features. Frequency analysis of inviscid simulations demonstrated that oscillations present in simple blunt jet configurations are attributable to a periodic, inviscid vortex shedding mechanism. Based on detailed pressure coefficient comparisons, the steady, inviscid simulations were shown to reasonably predict forces for a wide variety of SRP flows. With the completion of these validation studies, we can move towards application of this fast, robust, and automatic modeling tool for large SRP design studies, while remaining alert for the possibility of unsteadiness and viscous processes in these complex flows.

Acknowledgments

References

[1] Manning, R. M. and Adler, M., "Landing on Mars," AIAA Paper 2005-6742, AIAA SPACE 2005 Conference & Exposition, Long Beach, CA, September 2005.

[2] Braun, R. D. and Manning, R. M., "Mars Exploration Entry, Descent, and Landing Challenges," *Journal of Spacecraft and Rockets*, Vol. 44, No. 2, March-April 2007, pp. 310–323.

[3] Edquist, K. T., Dyakonov, A. A., Korzun, A. M., Shidner, J. D., Studak, J. W., Tigges, M. A., Kipp, D. M., Prakash, R., Trumble, K. A., and Dupzyk, I. C., "Development of Supersonic Retro-Propulsion for Future Mars Entry, Descent, and Landing Systems," AIAA Paper 2010-5046, AIAA/ASME Joint Thermophysics and Heat Transfer Conference, Chicago, IL, July 2010.

[4] Love, E. S. and Grigsby, C. E., "Some Studies of Axisymmetric Free Jets Exhausting From Sonic and Supersonic Nozzles Into Still Air and Into Supersonic Streams," NACA Research Memorandum NACA-RM-L54L31, Langley Aeronautical Laboratory, Langley Field, VA, May 1955.

[5] Hayman, L. O. and McDearmon, Jr., R. W., "Jet Effects on Cylindrical Afterbodies Housing Sonic and Supersonic Nozzles Which Exhaust Against a Supersonic Stream at Angles of Attack from 90° to 180°," NASA Technical Note NASA-TN-D-1016, Langley Research Center, Langley Air Force Base, VA, March 1962.

^{6}Peterson, V. L. and McKenzie, R. L., "Effects of Simulated Retrorockets on the Aerodynamic Characteristics of a Body of Revolution at Mach Numbers from 0.25 to 1.90," NASA Technical Note D-1300, Ames Research Center, Moffett Field, CA, May 1962.

^{7}Keyes, J. W. and Hefner, J. N., "Effect of Forward-Facing Jets on Aerodynamic Characteristics of Blunt Configurations at Mach 6," *Journal of Spacecraft*, Vol. 4, No. 4, April 1967, pp. 533–534.

^{8}Jarvinen, P. O. and Adams, R. H., "The Effects of Retrorockets on the Aerodynamic Characteristics of Conical Aeroshell Planetary Entry Vehicles," AIAA Paper 70-219, AIAA 8th Aerospace Sciences Meeting, New York, NY, January 1970.

^{9}Jarvinen, P. O. and Adams, R. H., "The Aerodynamic Characteristics of Large Angled Cones with Retrorockets," NASA Contract No. NAS7-576, Cambridge, MA, Feb. 1970.

^{10}McGhee, R. J., "Effects of a Retronozzle Located at the Apex of a 140° Blunt Cone at Mach Numbers of 3.00, 4.50, and 6.00," NASA Technical Note NASA-TN-D-6002, Langley Research Center, Hampton, VA, January 1971.

^{11}Grenich, A. F. and Woods, W. C., "Flow Field Investigation of Atmospheric Braking for High Drag Vehicles with Forward Facing Jets," AIAA Paper 1981-0293, 19th AIAA Aerospace Sciences Meeting, St. Louis, MO, January 1981.

^{12}Menezes, V., Saravanan, S., Jagadeesh, G., and Reddy, K. P. J., "Experimental Investigations of Hypersonic Flow over Highly Blunted Cones with Aerospikes," *AIAA Journal*, Vol. 41, No. 10, October 2003, pp. 1955–1966.

^{13}Meyer, B., Nelson, H. F., and Riggins, D. W., "Hypersonic Drag and Heat-Transfer Reduction using a Forward-Facing Jet," *Journal of Aircraft*, Vol. 38, No. 4, July-August 2001, pp. 680–686.

^{14}Hatashi, K., Aso, S., and Tani, Y., "Numerical Study of Thermal Protection System by Opposing Jet," AIAA Paper 2005-188, 43rd AIAA Aerospace Sciences Meeting, Reno, NV, January 2005.

^{15}Chang, C.-L., Venkatachari, B. S., and Cheng, G. C., "Effect of Counterflow Jet on a Supersonic Reentry Capsule," AIAA Paper 2006-4776, 42nd AIAA/ASME/SAE/ASEE Joint Propulsion Conference, Sacramento, CA, July 2006.

^{16}Daso, E. O., Pritchett, V. E., Wang, T.-S., Ota, D. K., Blankson, I. M., and Auslender, A. H., "The Dynamics of Shock Dispersion and Interactions in Supersonic Freestreams with Counterflowing Jets," AIAA Paper 2007-1423, 45th AIAA Aerospace Sciences Meeting, Reno, NV, January 2007.

^{17}Shang, J. S., "Plasma Injection for Hypersonic Blunt-Body Drag Reduction," *AIAA Journal*, Vol. 40, No. 6, June 2002, pp. 1178–1186.

^{18}Stalder, J. R. and Inouye, M., "A Method of Reducing Heat Transfer to Blunt Bodies by Air Injection," NACA Research Memorandum NACA-RM-A56B27a, Ames Aeronautical Laboratory, Moffett Field, CA, May 1956.

^{19}Romeo, D. J. and Sterrett, J. R., "Flow Field for Sonic Jet Exhausting Counter to a Hypersonic Mainstream," *AIAA Journal*, Vol. 3, No. 3, March 1965, pp. 544–546.

^{20}Finley, P. J., "The Flow of a Jet from a Body Opposing a Supersonic Free Stream," *Journal of Fluid Mechanics*, Vol. 26, No. 2, 1966, pp. 337–368.

^{21}Korzun, A. M., Cruz, J. R., and Braun, R. D., "A Survey of Supersonic Retropropulsion Technology for Mars Entry, Descent, and Landing," *Journal of Spacecraft and Rockets*, Vol. 46, No. 5, September-October 2009, pp. 929–937.

^{22}Drake, B. G. (Editor), "Reference Mission Version 3.0, Addendum to the Human Exploration of Mars: The Reference Mission of the NASA Mars Exploration Study Team," NASA SP-6107-ADD, Exploration Office, NASA Johnson Space Center, June 1998.

^{23}Drake, B. G. (Editor), "Human Exploration of Mars, Design Reference Architecture 5.0," NASA SP-2009-566, Mars Architecture Steering Group, NASA Headquarters, July 2009.

^{24}Drake, B. G. (Editor), "Human Exploration of Mars, Design Reference Architecture 5.0: Addendum," NASA SP-2009-566-ADD, Mars Architecture Steering Group, NASA Headquarters, July 2009.

^{25}Bakhtian, N. M. and Aftosmis, M. J., "Maximum Attainable Drag Limits for Atmospheric Entry via Supersonic Retropropulsion," *Proceedings of the 8th International Planetary Probe Workshop*, Portsmouth, VA, June 2011.

^{26}Zang, T. A. (Editor), "Entry, Descent and Landing Systems Analysis Study: Phase 1 Report," NASA TM-2010-216720, EDL Systems Analysis Team, May 2010.

^{27}Bakhtian, N. M. and Aftosmis, M. J., "Parametric Study of Peripheral Nozzle Configurations for Supersonic Retropropulsion," AIAA Paper 2010-1239, 48th AIAA Aerospace Sciences Meeting, Orlando, FL, January 2010.

^{28}Trumble, K. A., Schauerhamer, D. G., Kleb, W. L., Carlson, J.-R., Buning, P. G., Edquist, K., and Barnhardt, M. D., "An Initial Assessment of Navier-Stokes Codes Applied to Supersonic Retro-Propulsion," AIAA Paper 2010-5047, AIAA/ASME Joint Thermophysics and Heat Transfer Conference, Chicago, IL, July 2010.

^{29}Korzun, A. M., Cordell, C. E., and Braun, R. D., "Comparison of Inviscid and Viscous Aerodynamic Predictions of Supersonic Retropropulsion Flowfields," AIAA Paper 2010-5048, AIAA/ASME Joint Thermophysics and Heat Transfer Conference, Chicago, IL, July 2010.

^{30}Alkandry, H., Boyd, I. D., Reed, E. M., Codoni, J. R., and McDaniel, J. S., "Interactions of Single-Nozzle Sonic Propulsive Deceleration Jets on Mars Entry Aeroshells," AIAA Paper 2010-4888, AIAA/ASME Joint Thermophysics and Heat Transfer Conference, Chicago, IL, July 2010.

^{31}Schauerhamer, D. G., "Ongoing Study of Supersonic Retro-Propulsion Using Structured Overset Grids and OVERFLOW," Presentation, 10th Symposium on Overset Composite Grids and Solution Technology, Moffett Field, CA, September 2010.

^{32}Bakhtian, N. M. and Aftosmis, M. J., "Parametric Study of Peripheral Nozzle Configurations for Supersonic Retropropulsion," *Journal of Spacecraft and Rockets*, Vol. 47, No. 6, November-December 2010, pp. 935–950.

^{33}Alkandry, H., Boyd, I. D., Reed, E. M., Codoni, J. R., and McDaniel, J. S., "Interactions of Single-Nozzle Supersonic Propulsive Deceleration Jets on Mars Entry Aeroshells," AIAA Paper 2011-138, 49th AIAA Aerospace Sciences Meeting, Orlando, FL, January 2011.

^{34}Codoni, J. R., Reed, E. M., McDaniel, J. S., Alkandry, H., and Boyd, I. D., "Investigations of Peripheral 4-jet Sonic and Supersonic Propulsive Deceleration Jets on a Mars Science Laboratory Aeroshell," AIAA Paper 2011-1036, 49th AIAA Aerospace Sciences Meeting, Orlando, FL, January 2011.

[35]Trumble, K. A., Schauerhamer, D. G., Kleb, W. L., Carlson, J.-R., and Edquist, K. T., "Analysis of Navier-Stokes Codes Applied to Supersonic Retro-Propulsion Wind Tunnel Test," IEEEAC 1471, IEEE Aerospace Conference, Big Sky, MT, March 2011.

[36]Cordell, C. E., Clark, I. G., and Braun, R. D., "CFD Verification of Supersonic Retropropulsion for a Central and Peripheral Configuration," IEEEAC 1190, IEEE Aerospace Conference, Big Sky, MT, March 2011.

[37]Schauerhamer, D. G., Trumble, K. A., Kleb, W. L., Carlson, J.-R., Edquist, K. T., Buning, P. G., and Sozer, E., "Ongoing Validation of Computational Fluid Dynamics for Supersonic RetroPropulsion," *Proceedings of the 8th International Planetary Probe Workshop*, Portsmouth, VA, June 2011.

[38]Kleb, W. L., Schauerhamer, D. G., Trumble, K. A., Sozer, E., Barnhardt, M. D., Carlson, J.-R., and Edquist, K. T., "Toward Supersonic Retropropulsion CFD Validation," AIAA Paper 2011-TBD, 42th AIAA Thermophysics Conference, Honolulu, HI, June 2011.

[39]Korzun, A. M., Clark, I. G., and Braun, R. D., "Application of a Reynolds-Averaged Navier-Stokes Approach to Supersonic Retropropulsion Flowfields," AIAA Paper 2011-TBD, 29th AIAA Applied Aerodynamics Conference, Honolulu, HI, June 2011.

[40]Trumble, K. A., Kleb, W. L., Schauerhamer, D. G., Sozer, E., Barnhardt, M. D., Carlson, J.-R., Buning, P. G., and Edquist, K. T., "Progress Report: 4.4.4.1 Computational Fluid Dynamics Assessment," NASA Internal Report, Version 1.0, Supersonic Retropropulsion Element, Entry, Descent & Landing Project, Exploration Technology Development Program, June 2011.

[41]Berry, S. A., Laws, C. T., Kleb, W. L., Rhode, M. N., Spells, C., Mccrea, A. C., Trumble, K. A., Schauerhamer, D. G., and Oberkampf, W. L., "Supersonic Retro-Propulsion Experimental Design for Computational Fluid Dynamics Model Validation," IEEEAC 1499, IEEE Aerospace Conference, Big Sky, MT, March 2011.

[42]Berry, S. A., Rhode, M. N., Edquist, K. T., and Player, C. J., "Supersonic Retropropulsion Experimental Results from the NASA Langley Unitary Plan Wind Tunnel," AIAA Paper 2011-TBD, 42th AIAA Thermophysics Conference, Honolulu, HI, June 2011.

[43]Daso, E. O., Pritchett, V. E., Wang, T.-S., Ota, D. K., Blankson, I. M., and Auslender, A. H., "Dynamics of Shock Dispersion and Interactions in Supersonic Freestreams with Counterflowing Jets," *AIAA Journal*, Vol. 47, No. 6, June 2009, pp. 1313–1326.

[44]Nomura, H., Aso, S., and Nishida, M., "Numerical Simulation of Opposing Sonic Jets," *Computers and Fluids*, Vol. 21, No. 2, 1992, pp. 229–233.

[45]Adamson, Jr., T. C. and Nicholls, J. A., "Final Report: On the Structure of Jets from Highly Underexpanded Nozzles Into Still Air," Department of the Army, Detroit Ordnance District, ERI Project 2397 No. DA-20-018-ORD-13821, Engineering Research Institute, University of Michigan, Detroit, Michigan, February 1958.

[46]Norman, M. L. and Winkler, K.-H. A., "Supersonic Jets," *Los Alamos Science*, Vol. Spring/Summer, No. 12, 1985, pp. 38–71.

[47]Aftosmis, M. J., Berger, M. J., and Melton, J. E., "Robust and Efficient Cartesian Mesh Generation for Component-Based Geometry," *AIAA Journal*, Vol. 36, No. 6, 1998, pp. 952–960.

[48]Aftosmis, M. J., Berger, M. J., and Adomavicius, G., "A Parallel Multilevel Method for Adaptively Refined Cartesian Grids with Embedded Boundaries," AIAA Paper 2000-0808, 38th AIAA Aerospace Sciences Meeting, Reno, NV, January 2000.

[49]Nemec, M. and Aftosmis, M. J., "Adjoint Error Estimation and Adaptive Refinement for Embedded-Boundary Cartesian Meshes," AIAA Paper 2007-4187, 18th AIAA Computational Fluid Dynamics Conference, Miami, FL, June 2007.

[50]Nemec, M. and Aftosmis, M. J., "Adjoint Sensitivity Computations for an Embedded-Boundary Cartesian Mesh Method," *Journal of Computational Physics*, Vol. 227, 2008, pp. 2724–2742.

[51]Nemec, M., Aftosmis, M. J., and Wintzer, M., "Adjoint-Based Adaptive Mesh Refinement for Complex Geometries," AIAA Paper 2008-0725, 46th AIAA Aerospace Sciences Meeting, Reno, NV, January 2008.

[52]Aftosmis, M. J., Berger, M. J., and Murman, S. M., "Applications of Space-Filling Curves to Cartesian Methods for CFD," AIAA Paper 2004-1232, 42nd AIAA Aerospace Sciences Meeting, Reno, NV, January 2004.

[53]Berger, M. J., Aftosmis, M. J., and Murman, S. M., "Analysis of Slope Limiters on Irregular Grids," AIAA Paper 2005-0490, 43rd AIAA Aerospace Sciences Meeting, Reno, NV, January 2005.

[54]Berger, M. J., Aftosmis, M. J., Marshall, D. D., and Murman, S. M., "Performance of a New CFD Flow Solver Using a Hybrid Programming Paradigm," *Journal of Parallel and Distributed Computing*, Vol. 65, No. 4, 2005, pp. 414–423.

[55]Aftosmis, M. J. and Rogers, S. E., "Effects of Jet-Interaction on Pitch Control of a Launch Abort Vehicle," AIAA Paper 2008-1281, 46th AIAA Aerospace Sciences Meeting, Reno, NV, January 2008.

[56]Aftosmis, M. J. and Nemec, M., "Exploring Discretization Error in Simulation-Based Aerodynamic Databases," *Proceedings of the 21st International Conference on Parallel Computational Fluid Dynamics*, edited by R. Biswas, DEStech Publications, Inc., May 2009.

[57]Murman, S. M., Aftosmis, M. J., and Nemec, M., "Automated Parameter Studies Using a Cartesian Method," NAS Technical Report NAS-04-015, NASA Ames Research Center, Moffett Field, CA, November 2004.

[58]Venditti, D. A. and Darmofal, D. L., "Grid Adaptation for Functional Outputs: Application to Two-Dimensional Inviscid Flows," *Journal of Computational Physics*, Vol. 176, 2002, pp. 40–69.

[59]Wintzer, M., Nemec, M., and Aftosmis, M. J., "Adjoint-Based Adaptive Mesh Refinement for Sonic Boom Prediction," AIAA Paper 2008-6593, 26th AIAA Applied Aerodynamics Conference, Honolulu, HI, August 2008.

[60]Jameson, A., "Time Dependent Calculations Using Multigrid, with Applications to Unsteady Flows Past Airfoils and Wings," AIAA Paper 1991-1596, 10th AIAA Computational Fluid Dynamics Conference, Honolulu, HI, June 1991.

[61]Melson, N. D., Sanetrik, M. D., and Atkins, H. L., "Time-Accurate Navier-Stokes Calculations with Multigrid Acceleration," *Proceedings of the Sixth Copper Mountain Conference on Multigrid Methods*, April 1993.

[62]Murman, S. M., Aftosmis, M. J., and Berger, M. J., "Implicit Approaches for Moving Boundaries in a 3-D Cartesian Method," AIAA Paper 2003-1119, 41st AIAA Aerospace Sciences Meeting, Reno, NV, January 2003.

[63]Murman, S. M., Aftosmis, M. J., and Berger, M. J., "Numerical Simulation of Rolling-Airframes Using a Multi-Level Cartesian Method," AIAA Paper 2002-2798, 20th AIAA Applied Aerodynamics Conference, St. Louis, MO, June 2002.

[64]Wright, M. W., White, T., and Mangini, N., "Data Parallel Line Relaxation (DPLR) Code user Manual Acadia - Version 4.01.1," NASA Technical Memorandum TM-2009-215388, October 2009.

[65]Nichols, R. H., Tramel, R. W., and Buning, P. G., *Users Manual for OVERFLOW 2.1*, 2008.

[66]Buning, P. G., Chiu, I. T., Obayashi, S., Rizk, Y. M., and Steger, J. L., "Numerical Simulation of the Integrated Space Shuttle Vehicle in Ascent," AIAA Paper 88-4359, AIAA Atmospheric Flight Mechanics Conference, Minneapolis, MN, August 1988.

[67]Jespersen, D. C., Pulliam, T. H., and Buning, P. G., "Recent enhancements to OVERFLOW," AIAA Paper 97-0644, 35th AIAA Aerospace Sciences Meeting, Reno, NV, January 1997.

[68]Nichols, R. H., Tramel, R. W., and Buning, P. G., "Solver and Turbulence Model upgrades to OVERFLOW 2 for Unsteady and High-Speed Applications," AIAA Paper 2006-2824, 24th Applied Aerodynamics Conference, San Francisco, CA, June 2006.

[69]Anderson, W. K. and Bonhaus, D. L., "An Implicit Upwind Algorithm for Computing Turbulent Flows on Unstructured Grids," *Computers and Fluids*, Vol. 23, No. 1, 1994, pp. 1–21.

[70]Anderson, W. K., Rausch, R. D., and Bonhaus, D. L., "Implicit/Multigrid Algorithm for Incompressible Turbulent Flows on Unstructured Grids," *Journal of Computational Physics*, Vol. 128, No. 2, 1996, pp. 391–408.